AGU PUBLICATIONS

JGR

Journal of Geophysical Research: Space Physics

RESEARCH ARTICLE
10.1002/2014JA019931

Key Points:
- Quiet plasma sheet ECH wave emissions exhibit preference for dawn
- ECH waves are more confined to equator with reduced local plasma sheet activity
- ECH wave Z-extent is linearly correlated with field line curvature radius

Correspondence to:
X.-J. Zhang,
xjzhang@ucla.edu

Citation:
Zhang, X.-J., V. Angelopoulos, B. Ni, R. M. Thorne, and R. B. Horne (2014), Extent of ECH wave emissions in the Earth's magnetotail, *J. Geophys. Res. Space Physics*, *119*, 5561–5574, doi:10.1002/2014JA019931.

Received 27 FEB 2014
Accepted 25 JUN 2014
Accepted article online 27 JUN 2014
Published online 21 JUL 2014

Extent of ECH wave emissions in the Earth's magnetotail

Xiaojia Zhang[1], Vassilis Angelopoulos[1], Binbin Ni[2,3], Richard M. Thorne[3], and Richard B. Horne[4]

[1]Department of Earth, Planetary, and Space Sciences and Institute of Geophysics and Space Physics, University of California, Los Angeles, California, USA, [2]Department of Space Physics, School of Electronic Information, Wuhan University, Wuhan, Hubei, China, [3]Department of Atmospheric and Oceanic Sciences, University of California, Los Angeles, California, USA, [4]British Antarctic Survey, Natural Environment Research Council, Cambridge, UK

Abstract The exact role of electrostatic electron cyclotron harmonic (ECH) waves in driving diffuse aurora has been controversial for many years. Using THEMIS observations from five magnetotail seasons, we investigate the occurrence rate distribution of ECH waves and the extent of individual wave intensifications under various plasma sheet conditions. Both are critical for modeling these waves' contributions to electron scattering and to diffuse auroral emissions. Single-spacecraft data analysis shows that ECH waves occur frequently in the midnight and postmidnight magnetotail and that their occurrence rates decrease with increasing radial distance from Earth. More than 50% of ECH wave events (continuous intervals of wave activity) occur during local plasma sheet activations, evidenced by energetic electron injections and dipolarization fronts. Excluding ECH wave emissions concurrent with such local plasma sheet activations (known to peak in occurrence rate near premidnight), we find that quiet plasma sheet ECH wave emissions exhibit preference for dawn. This preference suggests a close relationship between these waves and the drift paths of injected electrons. Dual-spacecraft data analysis shows that the Z-extent is ~0.5 R_E, the Y-extent is ~2 R_E, and the X-extent is at least 4 R_E. During locally quiet plasma sheet conditions, ECH waves exhibit a smaller Z- and X-extent, but the Y-extent is similar during all the conditions. In order to investigate the mechanism leading to the different Z-extents under various plasma sheet conditions, we use ray tracing to model the wave power distribution as a function of distance from the neutral sheet. We find a linear correlation between the wave Z-extent and field line curvature radius (R_c). A Z-extent of ~0.2 R_E (consistent with observations) corresponds to R_c~0.9 R_E. Our results suggest that ECH intensification following dipolarizing flux bundles is in part due to increased R_c, which enables intensification to higher amplitudes over a larger volume, explaining the increased occurrence rate and extent of active-time wave events.

1. Introduction

Diffuse aurora dominates the hemispheric energy flux precipitating into the ionosphere, more than three quarters of which is contributed by electron precipitation [*Newell et al.*, 2009]. The diffuse auroral region extends over a 5° to 10° latitude range around the auroral oval and maps to the entire central plasma sheet. It is generally accepted that diffuse electron precipitation is caused by pitch-angle scattering of central plasma sheet electrons (hundreds to several thousand eV) into the atmospheric loss cone by wave-particle interactions [*Fontaine and Blanc*, 1983].

Electron cyclotron harmonic (ECH) waves, electrostatic emissions at frequencies between harmonics of the electron gyrofrequency (f_{ce}) [*Kennel et al.*, 1970; *Roeder and Koons*, 1989; *Meredith et al.*, 2009], have long been considered a candidate to drive such precipitation through cyclotron resonant scattering [*Kennel et al.*, 1970; *Lyons*, 1974]. In studying the generation mechanism of these waves, most researchers assumed a specific (unstable) distribution function and analyzed its consequences using the dispersion relation. Among the models used, the "loss cone distribution" has been extensively used for instability studies, exploring parameters that are plausible in the Earth's magnetosphere. ECH waves are thus thought to be generated by loss cone instability of the ambient, hot plasma sheet electron distribution in the presence of a low-density cold component [*Ashour-Abdalla and Kennel*, 1978; *Rönnmark and Christiansen*, 1981; *Horne et al.*, 1981; *Horne*, 1989; *Horne et al.*, 2003]. In the absence of distribution function measurements within the loss cone, and of cold electron measurements, which are both difficult to make but needed to guide further development in theory, this ECH excitation mechanism has not been verified. Despite the inability to measure all electron populations

and the loss cone anisotropy responsible for the scattering, parametric studies of growth as a function of these variables have been explored and are consistent with the wave properties. In particular, using typical values of the electron gyrofrequency, electron density, and loss cone size in the plasma sheet, *Ni et al*. [2012] have been able to reproduce the unstable wave frequencies and wave normal angles consistent with observations. Statistical studies on the global distribution of ECH waves have shown that they are confined near the magnetic equator and are seen most frequently in the night and dawn regions (~2100–0600 magnetic local time (MLT)) for $4 < L < 10$ [*Roeder and Koons*, 1989; *Meredith et al*., 2009; *Ni et al*., 2011a].

The exact role of ECH waves in diffuse auroral precipitation has been controversial for over 4 decades [e.g., *Kennel et al*., 1970; *Lyons*, 1974; *Belmont et al*., 1983; *Roeder and Koons*, 1989; *Horne and Thorne*, 2000; *Horne et al*., 2003; *Meredith et al*., 2009]. Based on a detailed analysis of CRRES data and quasi-linear modeling, *Thorne et al*. [2010], *Ni et al*. [2011b], and *Tao et al*. [2011] have demonstrated that whistler mode chorus emissions are the dominant mechanism for diffuse auroral precipitation for $L < 7$. However, the occurrence of chorus drops substantially at larger L [*Li et al*., 2009, 2010]; recent studies have shown that ECH waves could be the dominant driver of diffuse auroral precipitation in the outer magnetosphere [*Ni et al*., 2011a, 2012; *Zhang et al*., 2013], beyond ~8 R_E, where high-latitude diffuse aurora [*Newell et al*., 2009, 2010] maps to.

To better examine the importance of ECH waves in driving diffuse aurora, quantitative evaluation of plasma sheet electron interactions with a more realistic wave model is required. The spatial distribution characteristics of ECH emissions have been reported using CRESS and THEMIS data [*Meredith et al*., 2009; *Ni et al*., 2011a]. However, these studies only utilized single spacecraft to evaluate the occurrence rates of these waves in space, without distinguishing the source location of each emission. Modeling the scattering effects of ECH waves and evaluating the specific contribution of ECH waves to diffuse aurora require understanding of the instantaneous wave spatial distribution with finer spatial resolution than can be derived from the single-spacecraft occurrence rate studies. Since intense waves appear to be absent most of the time and are likely localized, at least in Z (relative to the neutral sheet), a relative scale (established by two spacecraft) is far more informative than the occurrence rate spatial distribution established by single spacecraft.

The precipitated electron energy flux within the diffuse aurora is most intense from premidnight well into the morning hours [*Newell et al*., 2009]. But which characterization of ECH waves at the equator—as continuous, ubiquitous, small-amplitude emissions or impulsive, localized, strong ECH waves—contributes to such a precipitation pattern? And what do these characterizations tell us about the generation mechanism of these waves? Investigating directly the extent of ECH waves therefore can provide new insights into the origin of diffuse aurora.

Using the CRRES wave data, *Meredith et al*. [2000] demonstrated that ECH waves intensify significantly (with amplitudes at the magnetic equator above 1 mV/m) following substorm injections in the inner magnetosphere. Using the THEMIS data in the midtail region, *Zhang and Angelopoulos* [2014] established a temporal correlation between ECH wave events (continuous intervals of wave activity) and local plasma sheet activations, exemplified by electron injections or dipolarization fronts (DFs). This correlation suggests that the aforementioned phenomena can create plasma sheet conditions favorable for ECH wave growth in their aftermath, possibly due to reduced field line curvature and increased energy flux within a larger volume. Wave events not correlated with local injections and DFs at the spacecraft within an hour of wave observation, may be related to dawnward drifting electrons from a nearby injection. We hypothesize that along with these injected energetic electrons, resonant electron (in the several keV energy range) fluxes at the edge of the loss cone are also enhanced, contributing to ECH wave intensification along their drift paths. Dipolarization fronts and related injections are known to drive field-aligned currents [e.g., *Liu et al*., 2013] and discrete aurora [e.g., *Nakamura et al*., 2001; *Nishimura et al*., 2010]. In order to associate them with featureless diffuse auroras, we speculate that auroral precipitation can be diffuse at 1 MLT-MLAT spot, while field-aligned currents may cause discrete aurora elsewhere (probably westward of the diffuse auroral precipitation). In fact, we note that the Newell et al's study did not bin the precipitation data by activity index, but strictly by the type of spectrum observed, indicating that diffuse precipitation in that study could take place both during high *AE* index and concurrently with discrete precipitation (elsewhere in the auroral oval). Similarly, the plasma sheet can be locally "quiet" in that intense field-aligned currents

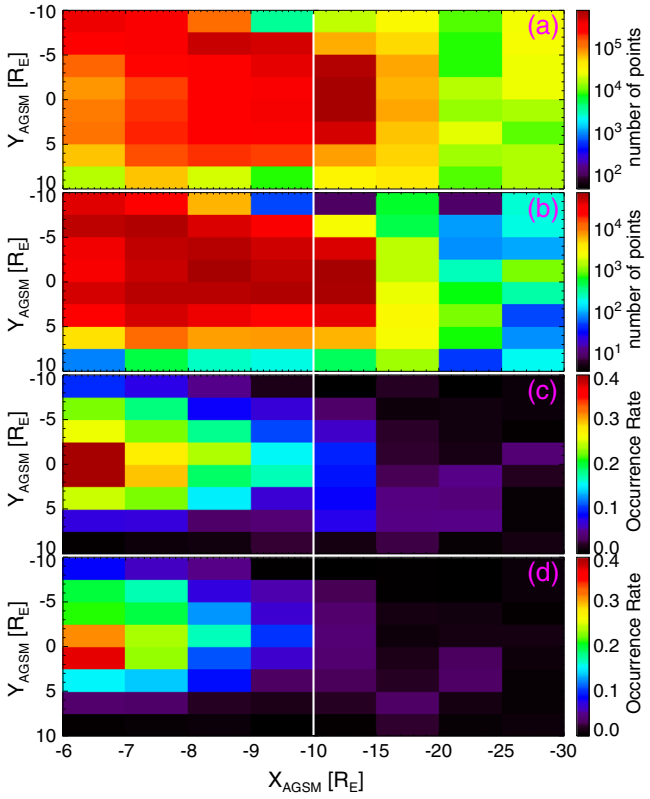

Figure 1. Distribution of (a) valid measurements (orbital distribution with valid EFI data within the central plasma sheet) and (b) ECH observations from single spacecraft in the *X-Y* plane (in aberrated GSM coordinates). (c) Occurrence rate of ECH emissions computed as the ratio of Figure 1b to Figure 1a. (d) Occurrence rate of ECH emissions that are not correlated with injections or DFs. Note that the spatial resolution changes from 1 R_E per tick on the left of the vertical white line to 5 R_E per tick on its right.

associated with DFs are absent at the observing spacecraft. Even though nearby bursty bulk flows encompassing one or more dipolarization fronts can be occurring, locally the quiet plasma sheet may still be the driver of diffuse aurora. We therefore segregate locally active plasma sheet intervals (times of injections and DFs) from quiet plasma sheet intervals (no injections or DFs) and assume that the latter represent quiet ionospheric conditions at the footprint. By examining the occurrence rate distribution and extent of ECH waves for active and quiet plasma sheet separately, we expect to improve our understanding of wave excitation under diverse magnetotail conditions.

With its prolonged residence in the plasma sheet, the THEMIS mission offers a unique data set for investigating ECH wave extent in more detail. By looking at the correlation of wave intensity between multiple spacecraft with different configurations and at various distances relative to each other or to the neutral sheet, we estimate the extent of these waves (if present) in different dimensions. By modeling the wave extent under different magnetic field topologies, we obtain further clues to the mechanism leading to wave intensification during/after injections/DFs.

We describe the database and how we evaluate the extent of selected ECH waves in section 2. Our observational results are shown in section 3. In section 4, we model the extent of these waves under different magnetic field configurations using the HOTRAY ray-tracing code to examine the relationship between the waves' extent and field topology. We summarize and discuss the results in sections 5 and 6.

2. Database and Methodology

THEMIS consists of five identical spacecraft (herein referred to as Probes P1, P2, P3, P4, and P5) equipped with comprehensive particle and field instruments [*Angelopoulos*, 2008]. Our database is derived from five THEMIS tail science phases (excluding intervals when the Electric Field Instrument wires were in the probe's shadow deeply enough to cause spikes in the raw waveforms that affect the onboard processed wave spectra), covering intervals from 15 December 2007 to 15 April 2008, 15 December 2008 to 15 April 2009, 2 March 2010 to 31 May 2010, 16 March 2011 to 22 June 2011, and 13 April 2012 to 14 October 2012. During the 2008 and 2009 tail seasons, the database contains measurements from all the five probes at different apogees [*Sibeck and Angelopoulos*, 2008]: P1 had an apogee of ~30 R_E; P2, ~20 R_E; and P3, P4, and P5, 10–12 R_E. Because P1 and P2 transited into lunar orbit from 2010 to 2012 (and have since been operating as the ARTEMIS mission), we only used the P3, P4, and P5 measurements with apogees at ~12 R_E. We exclude observations made when the probes were probably outside the magnetopause, when $\sqrt{Y^2+Z^2} \geq 12 R_E$ (GSM coordinates used in the

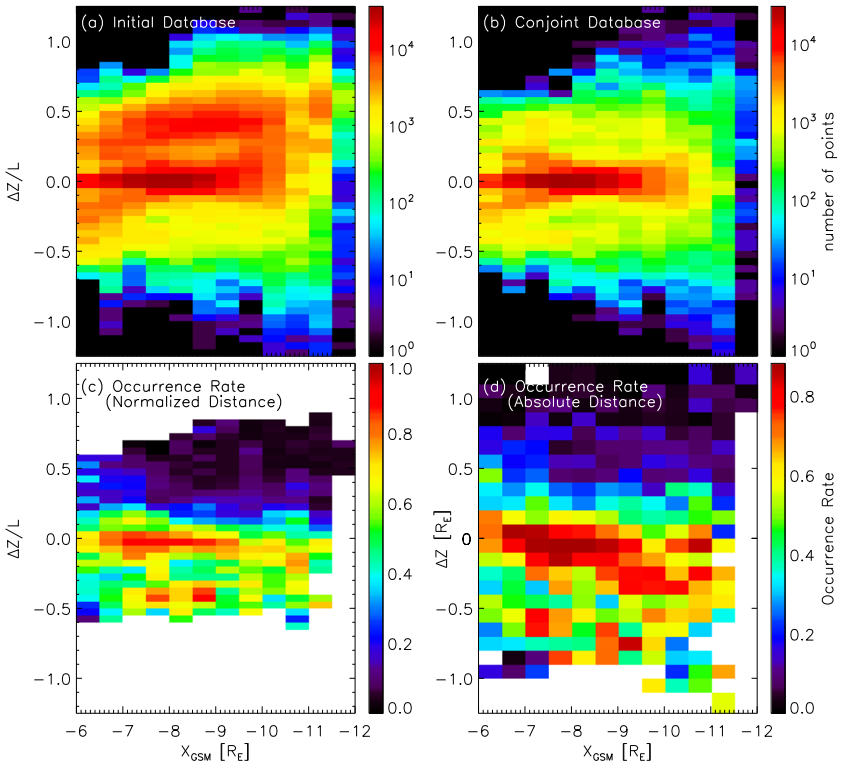

Figure 2. (a) Two-dimensional spatial distribution of dual-spacecraft measurements in the initial database, where one (the reference) spacecraft observes ECH waves and another (the second) spacecraft has valid measurements but may or may not observe the waves. The abscissa shows the X_{GSM} location (in R_E) of the reference spacecraft. The ordinate represents the spacecraft separation as the difference in normalized distance to the neutral sheet estimated by fitting the magnetic field data at the two spacecraft to a Harris sheet model. Normalization of distance to the neutral sheet is with respect to the current sheet thickness L. A positive value indicates that the second (other) spacecraft is in the direction away from the neutral sheet, and a negative value indicates that it is closer to the neutral sheet than the reference spacecraft. (b) Spatial distribution of the dual-spacecraft measurements in the conjoint database, where both the reference spacecraft and the other (second) spacecraft capture ECH waves at the same time. (c) Distribution of occurrence rates of ECH waves determined by the ratio of data in Figure 2b over Figure 2a. (d) Same as Figure 2c except that we used an absolute spacecraft distance in the Z direction after determining the thickness of the neutral sheet by fitting the data to a Harris sheet model (also see text). Note that when the number of observations in the initial database was fewer than 300, the ratios are not shown, to increase the statistical significance of the results and avoid noise.

paper unless otherwise specified). In addition, we exclude observations made when the probes were in the Earth's shadow.

The Electric Field Instrument (EFI) [*Bonnell et al.*, 2008] and the Search Coil Magnetometer (SCM) [*LeContel et al.*, 2008; *Roux et al.*, 2008] measure wave electric and magnetic fields in three orthogonal directions. Observations from EFI and SCM are passed to the Digital Fields Board (DFB) [*Cully et al.*, 2008] to calculate the mean amplitude of the electric and magnetic fields in six logarithmically spaced frequency bands from 0.1 Hz to 6 kHz, producing Filter Bank (FBK) data with a cadence of 4 s. FBK data are used in this study to select ECH events. The selection criteria are the same as developed by *Zhang and Angelopoulos* [2014], who organized ECH wave observations into contiguous sample intervals, termed "events," in order to investigate their correlation with injections and DFs. Their database includes 8753 ECH events in the plasma sheet with durations varying from 8 s to 3.9 h. In this study, we refer to the plasma sheet as the near-neutral sheet region of the plasma sheet (with plasma beta >0.5), where most ECH waves occur. Because of the potentially significant variation in spacecraft separation during an ECH event, we use all individual data samples (at 4 s resolution) within each wave event to investigate the spatial distribution and extent of ECH waves. We use measurements from all the five probes to show the spatial distribution of ECH waves from $X=-6\ R_E$ to $X=-30\ R_E$. Because of the large separations between the inner (P3, P4, and P5) and the

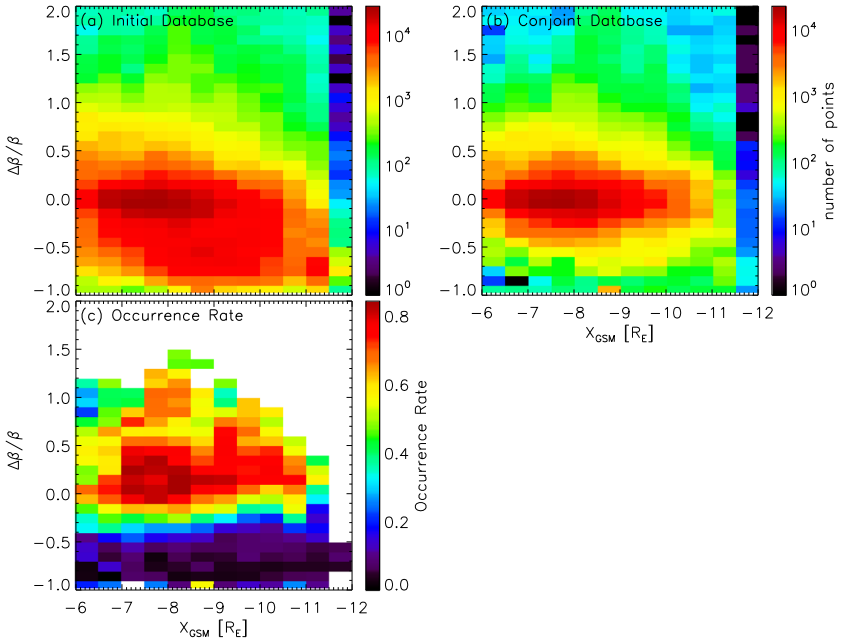

Figure 3. (a) Two-dimensional spatial distribution of dual-spacecraft measurements in the initial database, where one (the reference) spacecraft observes ECH waves and another (second) spacecraft has valid measurements but may or may not observe the waves. The abscissa shows the X_{GSM} location (in R_E) of the reference spacecraft. The ordinate represents the spacecraft separation as the normalized beta difference ($\Delta\beta$) between the two spacecraft. A negative value indicates that the second (other) spacecraft is in the direction away from the neutral sheet, and a positive value indicates that it is closer to the neutral sheet than the reference spacecraft. (b) Spatial distribution of the dual-spacecraft measurements in the conjoint database, where both the reference spacecraft and the other (second) spacecraft capture ECH waves at the same time. (c) Distribution of occurrence rates of ECH waves, determined by the ratio of data in Figure 3b over Figure 3a. Note that when the number of observations in the initial database was fewer than 300, the ratios are not shown, to increase the statistical significance of the results and avoid noise.

outer (P1 and P2) probes, which result in low correlation of wave intensities between inner and outer probes, we only use observations from the three inner probes to estimate the wave spatial scales.

We use observations from pairs formed by the three inner spacecraft. We select one spacecraft that observes ECH waves as the reference spacecraft. Then we separate the dual spacecraft observations according to whether the second spacecraft, assuming it has valid measurements, observes the waves at the same time. Within a certain spacecraft separation range, the ratio of samples of dual-spacecraft ECH observations to samples of single-spacecraft ECH observations (with the other spacecraft making valid plasma sheet measurements and thus having the potential to capture the waves if they are present) gives us the occurrence rate of ECH waves captured by two spacecraft. We refer to these two databases of single- and dual-spacecraft ECH wave emission samples as the "initial database" and the "conjoint database." The dual-spacecraft occurrence rate of ECH waves as a function of spacecraft separation in the *X* and *Y* directions provides the ECH wave extent in each dimension. With regard to estimating the wave occurrence rate as a function of distance from the neutral sheet (DNS), we note that the plasma sheet flaps and twists, and its hinge point varies with activity. Therefore, no magnetospheric model can provide a good estimate of neutral sheet location. We thus fit the in situ magnetic field data to a Harris sheet model [*Harris*, 1962] and use the model DNS to estimate spacecraft location and hence spacecraft separation in the *Z* direction. In addition, we compute the plasma beta (β), the thermal to magnetic pressure ratio, and treat the normalized beta difference ($\Delta\beta/\beta$) between the spacecraft as a proxy of their separation in the *Z* direction.

3. Observations

We first examine the spatial distribution of the wave occurrence rates at each spacecraft. As evident from Figure 1c, the occurrence rate of ECH emissions in the *X-Y* plane (in aberrated GSM coordinates with a 4° aberration angle) has a slight dawnward preference within 10 R_E, whereas ECH emissions are seen

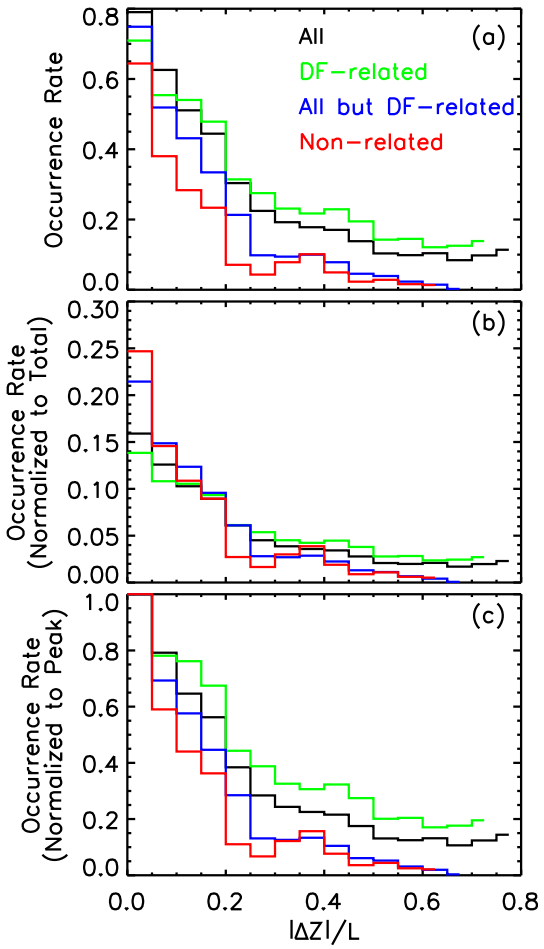

Figure 4. (a) Occurrence rate of dual-spacecraft observations of ECH waves as a function of $|\Delta Z|/L$: normalized occurrence rate with (b) the total and (c) the peak values within each category. These two normalizations allow us to see the relative distribution of wave occurrence within each category. The four traces in each plot represent the result for the entire wave database (black), the DF-related waves (green), the waves not correlated with DFs (blue), and the waves not correlated with DFs or injections (red). Note that when the number of observations in the initial database within each category was fewer than 4000, the occurrence rates are not shown, to increase the statistical significance of the results and avoid noise.

predominantly in the premidnight sector beyond 10 R_E. This premidnight preference beyond 10 R_E is correlated with higher geomagnetic activity (higher *AE* index, not shown here) in that region of the magnetotail. The occurrence rate of ECH emissions decreases with increasing distance from Earth, dropping to below 10% beyond 15 R_E. We also show the occurrence rate of ECH emissions that are not correlated with injections or DFs in Figure 1d (detailed definitions of this correlation can be found in *Zhang and Angelopoulos*, 2014). Compared to Figure 1c, these non-related ECH emissions have a clear preference for the dawn sector within 10 R_E.

We next examine the extent of ECH waves in the Z direction by recording the occurrence rate of dual-spacecraft observations for a certain Z separation (ΔZ) between the two spacecraft. In order to reduce the variation of wave occurrence due to the finite Y-extent of the wave emission region, we restrict the spacecraft separation to be Z dominated ($|\Delta Z_{GSM}| > |\Delta Y_{GSM}|$) when examining the Z-extent. Figures 2a and 2b show the spatial distribution of samples in the initial database (when the reference spacecraft sees the ECH waves and the other spacecraft is able to but does not necessarily observe the waves) and in the conjoint database, in the X-ΔZ plane. Here ΔZ was approximated by the difference of normalized distance to the neutral sheet (DNS) in a Harris sheet model fitted to the data. The normalization of DNS is with the current sheet thickness L. The ratio of the number of samples in the two databases is the occurrence rate of ECH emissions observed simultaneously at two locations separated by ΔZ, at a given distance from Earth, X. That ratio is shown in Figure 2c (for normalized ΔZ distances) and in Figure 2d (for absolute ΔZ distances, without normalizing to the current sheet thickness). We can see that the occurrence rate of ECH emissions is higher when the second spacecraft is closer to neutral sheet (negative ΔZ) than the reference spacecraft. Conversely, the occurrence rate is lower when the second spacecraft is farther away from the neutral sheet (positive ΔZ). Figure 2c shows that the maximum extent of ECH emissions in terms of normalized DNS is ~0.5. In absolute distances, the maximum scale is ~0.5 R_E.

In addition, we verify the Z-extent of ECH waves by using the relative change in plasma beta as a proxy of spacecraft separation in the Z direction. Figures 3a and 3b show the spatial distribution of samples in the initial database and conjoint database in the X-$\Delta\beta/\beta$ plane, where $\Delta\beta/\beta$, the normalized beta difference between two spacecraft, represents proximity to the neutral sheet. Consistent with Figures 2d and 2c, we can see that the occurrence rate of ECH emission capture (Figure 3c) is higher for the spacecraft closer to neutral sheet (positive $\Delta\beta/\beta$ indicates negative ΔZ) than for the spacecraft farther away from the neutral sheet (negative $\Delta\beta/\beta$ indicates positive ΔZ).

For better visualization and to compare different local plasma sheet activity conditions, we also show the occurrence rate of dual-spacecraft observations as a function of $|\Delta Z|/L$ in line plots (Figure 4). From Figure 4a,

we can see that the occurrence rate of observing simultaneous ECH emissions at two spacecraft drops to below 50% for spacecraft separations $|\Delta Z|/L > 0.18$; DF-related waves exhibit a similar trend, with slightly higher occurrence rates at larger $|\Delta Z|/L$; after excluding active plasma sheet conditions, i.e., ECH waves correlated with DFs (and injections), the occurrence rate decreases to below 50% when $|\Delta Z|/L > 0.13$ ($|\Delta Z|/L > 0.08$). This tendency for further equatorial localization of the waves with reduced local plasma sheet activity becomes clearer after normalizing the occurrence rates to the totals and peaks within each category. In Figures 4b and 4c, the DF-related, the non-DF, and the non-related (both non-DF and non-injection) categories are increasingly peaked at the narrowest equatorial bin, $|\Delta Z|/L < 0.05$, with steeper falloffs.

Finally, we examine the extent of ECH waves in the X and Y directions for different subsets. To eliminate aliasing due to the finite Z-extent, we only use the portion of the data for which the spacecraft separation ΔZ is negative, such that the other spacecraft is closer to the neutral sheet than the reference spacecraft. Figures 5a and 5b are histograms of the data in the initial and conjoint databases as a function of spacecraft separation in Y (ΔY_{GSM}). As shown in Figure 5c, which is derived from the ratio of the data in Figures 5b and 5a, the occurrence rate of dual ECH observations decreases significantly for $|\Delta Y_{GSM}| > 2\ R_E$ (for all the four subsets), indicating that the Y-scale of these waves is ~2 R_E. The normalized occurrence rates (Figures 5d and 5e) decrease more rapidly with $|\Delta Y_{GSM}|$ for non-related ECH waves than for the entire ECH database. In order to eliminate the variation of wave occurrence with Y separation, we further restricted the database with $|\Delta Y_{GSM}| \le 2\ R_E$ when examining the X-extent. Figures 5f and 5g are histograms of the data in the initial and conjoint databases as a function of spacecraft separation in X (ΔX_{GSM}). As shown in Figure 5h, the occurrence rate of dual ECH observations and simultaneous DF-related wave observations does not change much for $|\Delta X_{GSM}| \le 4\ R_E$. However, after excluding ECH waves correlated with DFs (and injections), we see a sharp decrease in the occurrence rate for $|\Delta X_{GSM}| > 1\ R_E$ in Figures 5h–5j.

4. Modeling

To better understand the results obtained above, we model the equatorial confinement of ECH waves under different magnetic field topologies. We use the HOTRAY ray-tracing code [*Horne*, 1989] to follow a group of rays launched with certain properties and estimate the Z-spread of each ray under a certain magnetic field topology.

We adopt a "modified" Harris sheet magnetic field topology by adding a uniform B_z component (B_{z0}) to the classic Harris sheet model:

$$\begin{aligned} B_x &= B_{x\text{lobe}} \cdot \tanh\left(\frac{Z}{L}\right) \\ B_z &= B_{z0} \end{aligned} \tag{1}$$

where $B_{x\text{lobe}}$ is the B_x component in the lobe, L is the half thickness of the current sheet, and Z is the distance to the neutral sheet. By varying $B_{x\text{lobe}}$ and L, which control the magnetic field curvature, we can model the wave propagation under different magnetic field topologies. We keep the magnetic field magnitude the same by normalizing electron gyrofrequency to a constant value of 365 Hz (consistent with that estimated from the data at midtail).

We employ an electron distribution with a partially filled loss cone that is consistent with the marginal instability state [*Zhang et al.*, 2013], represented by the sum of subtracted bi-Maxwellians [e.g., *Ashour-Abdalla and Kennel*, 1978; *Horne et al.*, 2003]:

$$f = \sum_i f_i,$$

where each component is expressed by

$$\begin{aligned} f_i\left(v_{//}, v_\perp\right) = {} & \frac{n_i}{\pi^{2/3}\alpha_{\perp i}^2 \alpha_{//i}} \exp\left(-\frac{v_{//}^2}{\alpha_{//i}^2}\right) \\ & \cdot \left[\Delta_i \exp\left(-\frac{v_\perp^2}{\alpha_{\perp i}^2}\right) + \frac{(1-\Delta_i)}{(1-\beta_i)} \cdot \left(\exp\left(-\frac{v_\perp^2}{\alpha_{\perp i}^2}\right) - \exp\left(-\frac{v_\perp^2}{\beta_i \alpha_{\perp i}^2}\right)\right)\right]. \end{aligned} \tag{2}$$

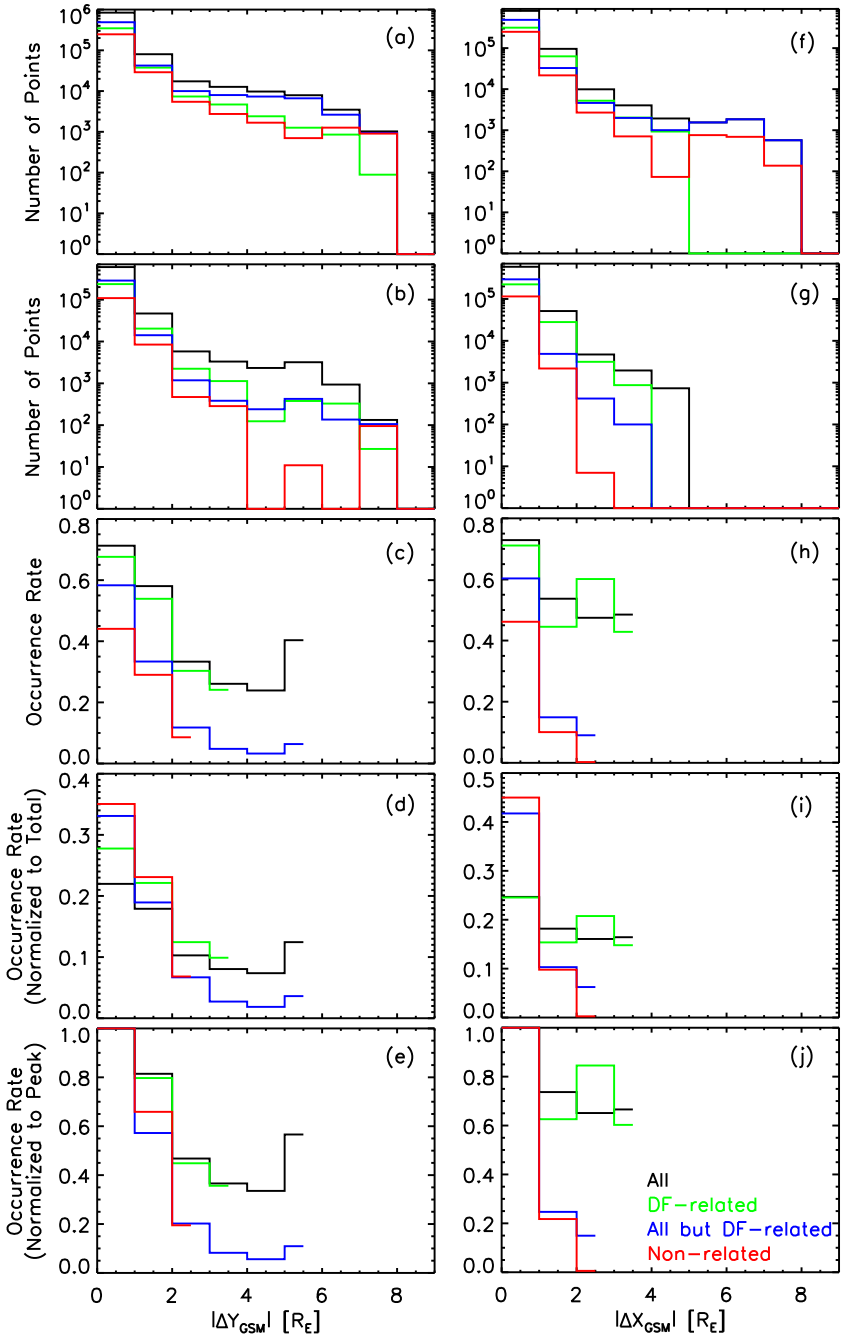

Figure 5. (a) and (f) Histograms of spacecraft separations in the Y and X directions ($\Delta Y_{GSM} = Y_{GSM,ref} - Y_{GSM,other}$ and $\Delta X_{GSM} = X_{GSM,ref} - X_{GSM,other}$, respectively) between the spacecraft that observes ECH waves (the reference spacecraft) and the other spacecraft, which has valid measurements but may or may not observe the waves. (b) and (g) Histograms of ΔY and ΔX separations only for cases when the other spacecraft also captures the waves at the same time as the reference spacecraft. (c) and (h) Occurrence rates of ECH waves as a function of ΔY and ΔX separations (the ratios of the values in Figures 5b and 5g over those in Figures 5a and 5f). (d) and (i) Distribution of normalized occurrence rates, the same occurrence rates as in Figures 5c and 5h except normalized such that the integral under each curve is unity. (e) and (j) Distribution of normalized occurrence rates to the peak values within each category. These two normalizations allow us to see the relative distribution of wave occurrence within each category. The four traces in each plot represent the result for the entire wave database (black), the DF-related waves (green), waves not correlated with DFs (blue), and waves not correlated with DFs or injections (red). Note that when the number of observations in the initial database within each category was fewer than 4000, the occurrence rates are not shown, to increase the statistical significance of the results and avoid noise.

Table 1. Parameters of Electron Components Used in the HOTRAY Ray-Tracing Code

Component	$N_e(m^{-3})$	$T_\perp(eV)$	$T_{//}(eV)$	Δ	β
1	6.04×10^4	3.10	3.10	1.0	0.5
2	3.02×10^5	338.6	214.5	0.255	0.163
3	2.42×10^5	1836.2	1163.4	0.027	0.047

Here n_i is the electron density, $\alpha_{\perp i}$ and $\alpha_{//i}$ are the thermal velocities perpendicular and parallel to the ambient magnetic field, and β_i and Δ_i essentially determine the depth and width of the loss cone, respectively. All the parameters are listed in Table 1, where the values of β_i and Δ_i provide a loss cone of ~1°, consistent with that calculated from the magnetic field data at midtail. In tracing rays under different magnetic field topologies, we use the same electron distribution and assume it to be constant with latitude and unchanging through the entire propagation region ($<1\ R_E$).

We first launch single ECH rays with the same wave frequency (1.2 f_{ce} has been used for the equatorial wave frequency based on typical observations of the ECH wave spectrum), but with a range of initial wave normal angles (in the growth regime, from 88.9° to 91.1°) and azimuthal angles (from 0° to 350°) at the equator. We then record the maximum Z-extent of these rays for a given magnetic field topology as represented by the radius of curvature and evaluate how representative that may be of the actual extent of the waves in the data. When they have propagated a short distance away from the neutral sheet, ECH waves typically refract because field line bending modifies the wave normal angle and thus the group velocity. Under different magnetic field configurations, these waves will refract at different latitudes, as indicated by the stars (linearly fitted by the green line) in Figure 8. The Z-extent of the rays is linearly correlated with the field line radius of curvature (R_c), and the R_c to Z-extent ratio is 16:1.

A radius of curvature of ~0.8 R_E, consistent with that expected from the data at midtail after the passage of a DF [*Li et al*., 2011], suggests that the waves should be confined within ~0.05 R_E of the neutral sheet, which implies that simultaneous observations of ECH waves between two spacecraft would have been scarce, given the large typical spacecraft separation along *Z* in our database (median separation is 0.3 R_E; only <7% of the data would have resulted in dual observations; yet our measured occurrence rate is 44%). This discrepancy is likely due to our oversimplified modeling of the ECH wave extent using single rays. In reality, the waves at a given location are the result of noise amplification emitted from a large range of source locations.

To study the wave amplification quantitatively in a more realistic scenario, we also model the distribution of ECH wave intensity as a function of distance to the neutral sheet by integrating at each observation point the wave power contribution from rays emanating from many different sources distributed uniformly in space. We adopt a similar methodology to previous work of modeling plasmaspheric hiss distribution from a given chorus source [*Bortnik et al*., 2011a, 2011b; *Chen et al*., 2012]. Specifically, we assume that the sources are distributed everywhere in the magnetotail, spaced at intervals of 0.1 R_E in *X*, 0.1 R_E in *Y*, and 0.1 R_E in Z. At each location, we launch rays with a fixed wave frequency (1.2 f_{ce}), but with a range of 0° to 180° of wave normal angles evenly distributed on the surface of the sphere. At each location and for each wave normal angle, we launch a set of azimuthal angles, from 0° to 350°, spaced at intervals of 10°. We launch $N = 1562 \times 36$ rays with various wave normal angles and azimuthal angles. As illustrated by five example sources labeled S0, S1, S2, S3, and S4 in Figure 6a, we propagate the rays away from the source. We then compute the power along the rays. Collecting the power from all the rays passing through a certain observation volume, with a half width of 0.05 R_E in *X*, 0.05 R_E in *Y*, and 0.01 R_E in Z, we assign the total power at the observation point to the center of that volume. For each ray at a given observation volume, the local intensity of the ray (normalized to its source intensity) is given by $\frac{P_i}{P_0} = \frac{10^{G/10}}{N}$, where *G* is the path-integrated gain from the launch location to the observation spot, *N* is the total number of rays launched at each origin, P_i and P_0 are the wave intensities at the observing and source locations. By repeating this for different observation locations systematically, we can build up the distribution of wave power everywhere in our one-dimensional model magnetotail.

Since free energy sources are assumed ubiquitous in our system, and since we adopt a field configuration that is uniform in the *X* and *Y* directions, wave growth continues indefinitely as the ray propagates away from its origin. Figure 7 shows the distribution of the power ratio at different distances away from an equatorial source. We restrict the range of wave propagation to ±1.0 R_E away from its source in both *X* and *Y*. We expect that magnetic field fluctuations violate the uniformity assumption and restrict further wave

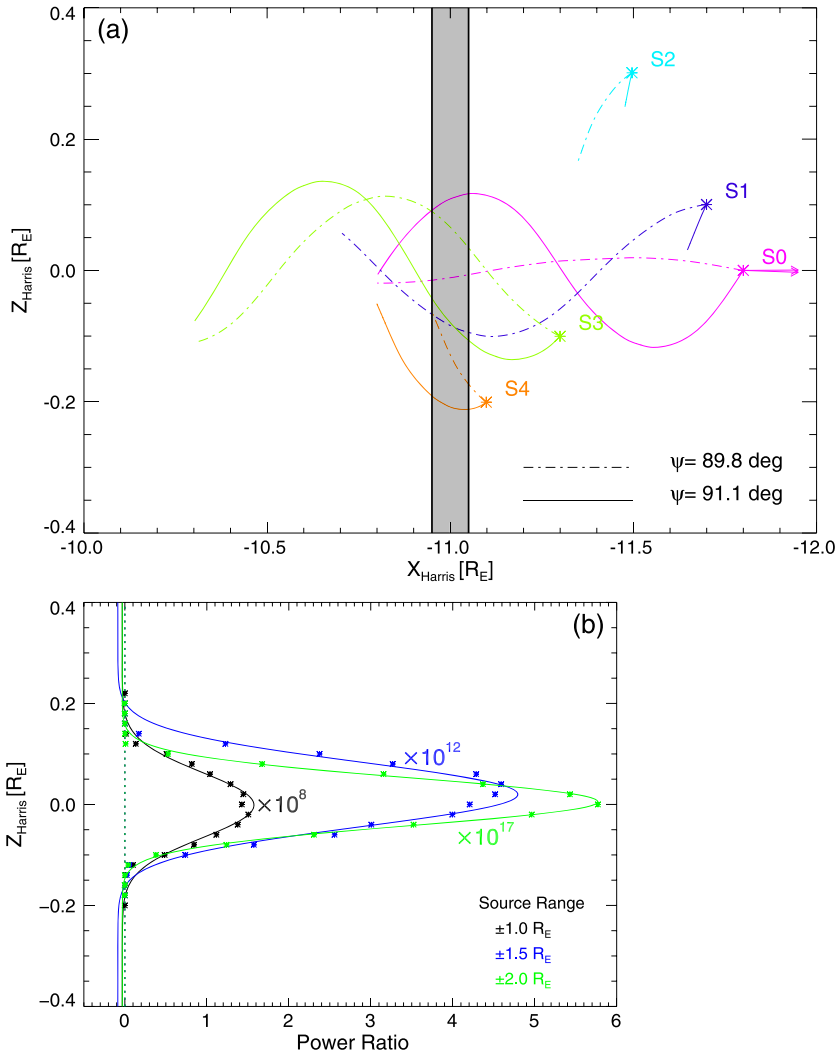

Figure 6. Schematic depicting our distributed, multisource modeling approach for ECH wave intensity reconstruction using ray tracing with the HOTRAY code. (a) *X-Z* projection of rays in our model. Sources are spaced at intervals of 0.1 R_E in *X*, *Y*, and *Z*. Only five sources are shown to exemplify the distributed sources. At each source, we launch multiple rays with a range of wave normal angles (rays that are able to propagate away from the origin have a limited range of wave normal angles from 88.9° to 91.1°) and different azimuthal angles (that affect the propagation direction in *Y*, but is not shown here). The two magenta arrows at source S_0 denote wave vector directions of the two exemplified rays. Wave growth due to loss cone instability and wave damping due to refraction of wave normal angles into a damped range controls the ray intensity as a function of the original intensity (which is assumed to start at noise level). The rays are collected and summed at each observer point (exemplified by the shaded region). (b) The summed wave power (relative to the source power) as a function of observer position in *Z*. The relative wave power is illustrated by the stars and exponentially fitted by the line. The colored curves represent results (each divided by the order of magnitude at the curve's peak) from different source range assumptions. The rays do not propagate farther than 0.2 R_E due to curvature. The vertical dotted line represents our selection of a threshold for the wave power ratio (10^{-4} of the peak wave power) on which to base our estimate of the Z-extent of the wave.

propagation beyond that distance by wave refraction and damping. Thus, rays from sources more than ±1.0 R_E away from an observation site are not allowed to contribute to wave power at that site.

Under our *X/Y* uniform field topology assumption, all sources radiate identically regardless of their *X/Y* location, so we need only to examine the wave power ratio distribution from sources located at different distances from the equator. So we construct forward tracing source models for rays launched at different distances from the equator, and this suffices for determining source behavior everywhere in the volume of interest. By back tracing ECH waves to different sources and summing up power ratios at each observation site, we obtain the

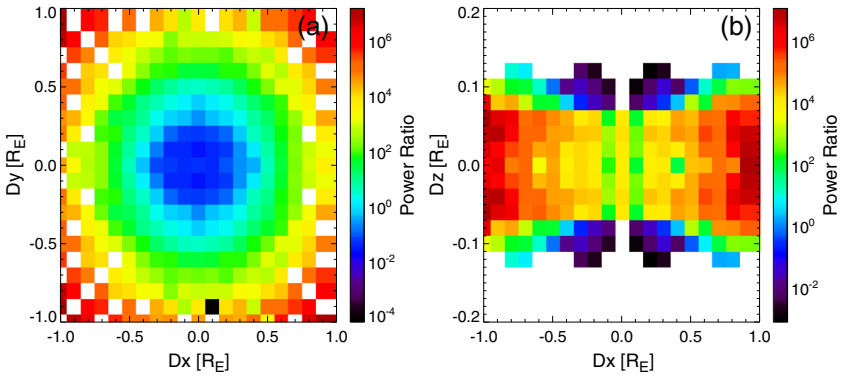

Figure 7. (a and b) Distribution of wave power ratio in our model as a function of distance from the source (this one launched at $Z = 0$) location. The model is a Harris sheet magnetic field modified by the addition of a finite B_z (B_{z0}) that establishes a field line curvature measured at the equator (for the case shown, $B_{z0} = 13$ nT, $L = 1.5$ R_E, $B_{xlobe} = 30$ nT, which results in $R_c = 0.8$ R_E).

wave power at observation sites with different Z but the same X and Y locations. The wave power profile is illustrated by the stars (exponentially fitted by the line) in Figure 6b for a certain field topology ($R_c = 0.8$ R_E). By looking at the Z distance at which the power ratio decreases to 10^{-4} of its equatorial maximum, we estimate the extent of the waves in this multisource model to be 0.18 R_E. We also estimate the Z-extent by restricting the range of wave propagation to ±1.5 R_E and ±2.0 R_E away from its source in both X and Y, as shown in Figure 6b. The resulting Z-extents are 0.16 R_E and 0.15 R_E, respectively. The Z-extent of the emission is roughly the same, regardless of the allowable range of the sources. Although the absolute amplification of the waves depends on the amplitude and wavelength of low-frequency plasma sheet fluctuations that may limit the region of ray propagation, the Z-extent is expected to be independent of our source range assumptions, because it is defined relative to peak amplification at the equator.

In the interest of saving running time, we only estimate the Z-extent of ECH waves under three different R_cs (0.8, 1.5, and 3.7 R_E); results are shown in Figure 8. The linear correlation between field line curvature and Z-extent, already established in the single ray-tracing result, is also evident in the multisource model results. The linear fit to the multisource model (red line) corresponds to a larger wave extent for a given magnetic field curvature radius, compared to single-ray runs. The R_c to wave Z-extent ratio is now 8:1. The reason for this is the presence of sources at nonequatorial locations which attain sufficient amplification; this is a more realistic scenario than single-ray estimates of the wave Z-extent. The observed Z-extent of ~0.2 R_E (for both the entire database and the DF-related subset) corresponds to an R_c of ~0.9 R_E, which is a reasonable field line curvature for a wide range of plasma sheet conditions and distances from Earth. For quiet-time events, a smaller Z-extent (~0.1 R_E) corresponds to an R_c of ~0.1 R_E.

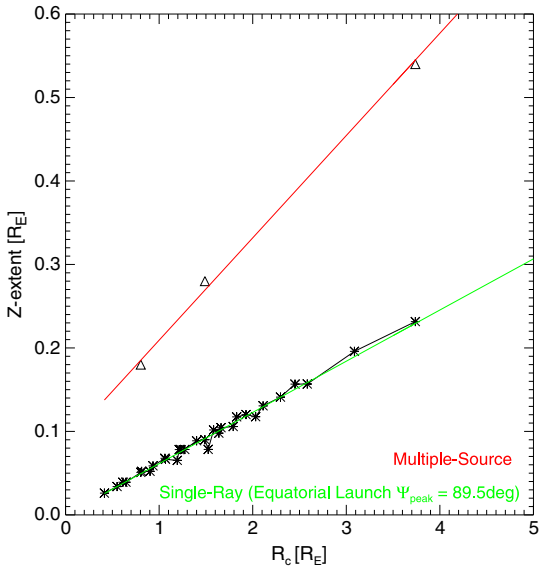

Figure 8. Maximum Z-extent of ECH waves as a function of the field line radius of curvature (R_c) from single-ray tracing (stars, linearly fitted by the green line) and multiple-source modeling (triangles, linearly fitted by the red line).

5. Summary

We used the five tail seasons of THEMIS observations to survey the spatial distribution of ECH emissions. As shown in Figure 1c, within 10 R_E, this distribution is almost symmetric across

the midnight meridian; beyond 10 R_E, ECH emissions occur preferentially in the premidnight region, which is correlated with higher geomagnetic activities. Within 10 R_E, the non-related (both non-DF and non-injection) ECH emissions show a clear preference for the dawn sector.

By correlating wave intensity between different THEMIS spacecraft, we estimated the extent of ECH waves in three directions. As consistently shown in Figures 2 and 3, the spacecraft closer to the neutral sheet tends to observe ECH waves more often than the one located farther away from the neutral sheet ($\Delta\beta/\beta$ and $\Delta Z/L$ are used as proxies of the spacecraft separation relative to the neutral sheet). As shown in Figures 2c and 2d, the maximum scale of ECH waves in Z is ~0.5 in terms of normalized DNS and ~0.5 R_E in absolute distance. We also compared the occurrence rate of dual-spacecraft observations as a function of $|\Delta Z|/L$ during different local plasma sheet activity conditions. With reduced local plasma sheet activity, ECH waves tend to be more confined to the equator (Figures 4b and 4c).

Similarly, we examined the extent of ECH waves in the X and Y directions for different subsets. As shown in Figure 5c, the Y-scale of these waves is ~2 R_E. The normalized occurrence rate (Figures 5d and 5e) of non-DF and non-related ECH waves decreases more rapidly with $|\Delta Y_{GSM}|$ than the occurrence rate in the entire database and in the DF-related subset. As shown in Figure 5h, the X-scale of the entire wave database and the DF-related subset is at least 4 R_E, whereas it decreases to ~1 R_E for the non-DF and non-related categories (Figures 5h–5j).

By tracing single ECH rays in the HOTRAY code, we found that the Z-extent of these rays is linearly correlated with the field line radius of curvature (R_c). We also modeled the distribution of ECH wave power as a function of distance to the neutral sheet by back tracing the waves to distributed sources in space, confirming the linear correlation between field line curvature and Z-extent and providing a realistic estimate of the wave extent for a given R_c. The observed Z-extent of ~0.2 R_E corresponds to an R_c of ~0.9 R_E, which is a reasonable value.

6. Discussion and Conclusion

The nearly symmetric occurrence of ECH waves across the midnight meridian within 10 R_E and the preference for the premidnight region beyond 10 R_E are consistent with previous statistical results from *Ni et al*. [2011a] in the overlap region of 6 to 15 R_E. After excluding ECH waves correlated with injections and DFs, which have been shown to peak in occurrence rate at premidnight [*Birn et al*., 1997; *Gabrielse et al*., 2013; *Liu et al*., 2013], we find that the non-related ECH emissions show a clear preference for the dawn sector (within 10 R_E). This may indicate that these waves are related to injected electrons that drift away from their original flow channels at premidnight.

Using simultaneous multiprobe observations, we established ECH waves' extent with finer scales than in single-spacecraft occurrence rate studies. In examining the Z-extent of these waves, we found a higher probability of observing ECH waves closer to the neutral sheet, which is expected from their equatorial confinement. Our results on the extent of the waves are expected to be used in future modeling of ECH wave interactions with plasma sheet electrons, which will enable better modeling of the precipitated electron energy flux for comparison with ground-based or ionospheric precipitation measurements. This, in turn, is expected to enable better evaluation of the contribution of ECH to diffuse aurora relative to other wave modes.

Our finding that the Z-extent of ECH waves is proportional to the magnetic field curvature radius (R_c) agrees with the hypothesis on the mechanism underlying the correlation between ECH waves and DFs reported by *Zhang and Angelopoulos* [2014]: when the magnetic field configuration becomes more dipolarized upon the arrival of dipolarizing flux bundles (the strong magnetic field region preceded by dipolarization fronts) [*Liu et al*., 2013], high-amplitude ECH waves will propagate to a greater latitudinal range around the neutral sheet, as indicated by Figure 8. The Z-extent of ECH waves from dual-spacecraft observations, ~0.2 R_E, corresponds to $R_c \sim 0.9\ R_E$ from our modeling, indicating that the observed extent of these waves is consistent with a dipolarized field topology [*Li et al*., 2011]. In addition, the strict confinement of ECH waves in Y ($\leq 2\ R_E$) and their loose confinement in X ($\geq 4\ R_E$) are consistent with the volume of a dipolarized flux tube after DFs pile up and dipolarization extends downtail [*Angelopoulos et al*., 1996]. This type of dipolarized flux region after DFs may be required to excite these waves to higher amplitudes over a sufficiently large extent in Z for them to be more easily observable in the aftermath of dipolarization fronts and injections, i.e., at active times.

By excluding ECH emissions correlated with injections and DFBs, we also examined the extent of these waves during quiet plasma sheet conditions. Waves not related to injections and DFBs (more stretched magnetic field topology) demonstrate a smaller Z-extent ($|\Delta Z|/L$~0.1) than those in the entire wave database, as shown in Figure 4. This agrees with our expectation that the curvature radius in a plasma sheet devoid of local dipolarizations would be smaller, leading to a smaller Z-extent of the waves. As shown in Figure 5, non-related ECH waves have a similar Y-extent (~2 R_E) but a smaller X-extent (~1 R_E) than those in the entire database (behavior dominated by DF-related waves). This further indicates that in addition to modifying the Z-extent of ECH waves by increasing the magnetic field curvature radius, dipolarizing flux bundles and related injections may also increase the wave X-extent by modifying the local magnetic topology and plasma environment; these modifications and their effects on wave generation are left for future investigation.

In modeling the wave power distribution, we restrict the range of wave propagation to ±1.0 R_E away from its source in both *X* and *Y*. Although this is an arbitrary cut, the Z-extent from modeling remains roughly the same when we vary this source range assumption. In addition, our model depicts a qualitative picture of why field line curvature (R_C) is critical to controlling the amplifications (and thus observations) of ECH waves. Verifications of our result will be pursued in a future study using a realistically varying magnetotail field topology.

Excited by the loss cone instability of the hot plasma sheet electrons, ECH waves can, in turn, scatter resonant electrons into the loss cone. There should be a quasi-steady state in which electron diffusion balances wave growth. Because of the smaller loss cones at higher *L* shells, ECH wave amplitude during such a quasi-steady state in the outer magnetotail may drop below current instrument detection level during quiet conditions [*Zhang et al.*, 2013]. Although possibly not detectable, these low-amplitude ECH waves could still contribute to drizzle precipitation of diffuse aurora during quiet times. On the other hand, ECH waves can be intensified by local plasma sheet activations, such as electron injections and DFBs, which create plasma sheet conditions favorable for wave growth in their aftermath [*Meredith et al.*, 2000; *Zhang and Angelopoulos*, 2014]. This study shows that the Z-extent of ECH waves is dictated by the magnetic field line curvature, indicating that a dipolarized flux region (following DFs or at the adjacent, thin quiet plasma sheet) may be required to excite these waves to such a larger amplitude wave with observable extent in *Z*. Electron injections, often associated with DFBs, are also capable of promoting wave growth, not only locally within their injection channels but also along the dawnward drifting paths of injected electrons (localized to within 4 R_E in *Y*). Intensified wave emissions following plasma sheet activity may dominate the wave observations in the outer magnetotail ($X < -10$ R_E), contributing to enhanced diffuse auroral precipitation in higher magnetic latitudes during such active times.

Acknowledgments

We thank L. Chen for useful discussions and J. Hohl for her help with editing. We acknowledge the NASA contract NAS5-02099 for the use of data from the THEMIS Mission and the NASA grant NNX12AD12G. We thank J.W. Bonnell and F.S. Mozer for the use of EFI data; D. Larson and R.P. Lin for the use of SST data; C.W. Carlson and J.P. McFadden for the use of ESA data; A. Roux and O. LeContel for the use of SCM data; and K.H. Glassmeier, U. Auster, and W. Baumjohann for the use of FGM data provided under the lead of the Technical University of Braunschweig and with financial support through the German Ministry for Economy and Technology and the German Center for Aviation and Space (DLR) under contract 50 OC 0302.

Masaki Fujimoto thanks Jan Blecki and another reviewer for their assistance in evaluating this paper.

References

Angelopoulos, V. (2008), The THEMIS Mission, *Space Sci. Rev.*, *141*, 5–34.

Angelopoulos, V., et al. (1996), Multipoint analysis of a bursty bulk flow event on April 11, 1985, *J. Geophys. Res.*, *101*(A3), 4967–4989, doi:10.1029/95JA02722.

Ashour-Abdalla, M., and C. F. Kennel (1978), Nonconvective and convective electron cyclotron harmonic instabilities, *J. Geophys. Res.*, *83*(A4), 1531–1543, doi:10.1029/JA083iA04p01531.

Belmont, G., D. Fontaine, and P. Canu (1983), Are equatorial electron cyclotron waves responsible for diffuse auroral electron precipitation?, *J. Geophys. Res.*, *88*(A11), 9163–9170, doi:10.1029/JA088iA11p09163.

Birn, J., M. F. Thomsen, J. E. Borovsky, G. D. Reeves, D. J. McComas, and R. Belian (1997), Characteristic plasma properties during dispersionless substorm injections at geosynchronous orbit, *J. Geophys. Res.*, *102*(A2), 2309–2324, doi:10.1029/96JA02870.

Bonnell, J. W., F. S. Mozer, G. T. Delory, A. J. Hull, R. Abiad, R. E. Ergun, C. M. Cully, V. Angelopoulos, and P. R. Harvey (2008), The Electric Field Instrument (EFI) for THEMIS, *Space Sci. Rev.*, *141*, 303–341, doi:10.1007/s11214-008-9469-2.

Bortnik, J., L. Chen, W. Li, R. M. Thorne, and R. B. Horne (2011a), Modeling the evolution of chorus waves into plasmaspheric hiss, *J. Geophys. Res.*, *116*, A08221, doi:10.1029/2011JA016499.

Bortnik, J., L. Chen, W. Li, R. M. Thorne, N. P. Meredith, and R. B. Horne (2011b), Modeling the wave power distribution and characteristics of plasmaspheric hiss, *J. Geophys. Res.*, *116*, A12209, doi:10.1029/2011JA016862.

Chen, L., W. Li, J. Bortnik, and R. M. Thorne (2012), Amplification of whistler-mode hiss inside the plasmasphere, *Geophys. Res. Lett.*, *39*, L08111, doi:10.1029/2012GL051488.

Cully, C. M., R. E. Ergun, K. Stevens, A. Nammari, and J. Westfall (2008), The THEMIS digital fields board, *Space Sci. Rev.*, *141*, 343–355, doi:10.1007/s11214-008-9417-1.

Fontaine, D., and M. Blanc (1983), A theoretical approach to the morphology and the dynamics of diffuse auroral zones, *J. Geophys. Res.*, *88*(A9), 7171–7184, doi:10.1029/JA088iA09p07171.

Gabrielse, C., V. Angelopoulos, A. Runov, and D. L. Turner (2013), Statistical characteristics of particle injections throughout the equatorial magnetotail, *J. Geophys. Res. Space Physics*, *119*, 2512–2535, doi:10.1002/2013JA019638.

Harris, E. G. (1962), On a plasma sheath separating regions of oppositely directed magnetic field, *Nuovo Cimento*, *23*, 115–121.

Horne, R. B. (1989), Path-integrated growth of electrostatic waves: The generation of terrestrial myriametric radiation, *J. Geophys. Res.*, *94*(A7), 8895–8909, doi:10.1029/JA094iA07p08895.

Horne, R. B., and R. M. Thorne (2000), Electron pitch angle diffusion by electrostatic electron cyclotron harmonic waves: The origin of pancake distributions, *J. Geophys. Res.*, *105*(A3), 5391–5402, doi:10.1029/1999JA900447.

Horne, R. B., P. J. Christiansen, M. P. Gough, K. Rönnmark, J. F. E. Johnson, J. Sojka, and G. L. Wrenn (1981), Amplitude variations of electron cyclotron harmonic waves, *Nature*, *294*, 338–340.

Horne, R. B., R. M. Thorne, N. P. Meredith, and R. R. Anderson (2003), Diffuse auroral electron scattering by electron cyclotron harmonic and whistler mode waves during an isolated substorm, *J. Geophys. Res.*, *108*(A7), 1290, doi:10.1029/2002JA009736.

Kennel, C., F. Scarf, R. Fredricks, J. McGehee, and F. Coroniti (1970), VLF electric field observations in the magnetosphere, *J. Geophys. Res.*, *75*(31), 6136–6152, doi:10.1029/JA075i031p06136.

LeContel, O., et al. (2008), First results of the THEMIS searchcoil magnetometers, *Space Sci. Rev.*, *141*, 509–534, doi:10.1007/s11214-008-9371-y.

Li, S.-S., V. Angelopoulos, A. Runov, X.-Z. Zhou, J. McFadden, D. Larson, J. Bonnell, and U. Auster (2011), On the force balance around dipolarization fronts within bursty bulk flows, *J. Geophys. Res.*, *116*, A00I35, doi:10.1029/2010JA015884.

Li, W., R. M. Thorne, V. Angelopoulos, J. Bortnik, C. M. Cully, B. Ni, O. LeContel, A. Roux, U. Auster and W. Magnes (2009), Global distribution of whistler-mode chorus observed on the THEMIS spacecraft, *Geophys. Res. Lett.*, *36*, L09104, doi:10.1029/2009GL037595.

Li, W., et al. (2010), THEMIS analysis of observed electron distributions responsible for chorus excitation, *J. Geophys. Res.*, *115*, A00F11, doi:10.1029/2009JA014845.

Liu, J., V. Angelopoulos, A. Runov, and X.-Z. Zhou (2013), On the current sheets surrounding dipolarizing flux bundles in the magnetotail: The case for wedgelets, *J. Geophys. Res. Space Physics*, *118*, 2000–2020, doi:10.1002/jgra.50092.

Lyons, L. (1974), Electron diffusion driven by magnetospheric electrostatic waves, *J. Geophys. Res.*, *79*(4), 575–580, doi:10.1029/JA079i004p00575.

Meredith, N. P., R. B. Horne, A. D. Johnstone, and R. R. Anderson (2000), The temporal evolution of electron distributions and associated wave activity following substorm injections in the inner magnetosphere, *J. Geophys. Res.*, *105*(A6), 12,907–12,917, doi:10.1029/2000JA900010.

Meredith, N. P., R. B. Horne, R. M. Thorne, and R. R. Anderson (2009), Survey of upper band chorus and ECH waves: Implications for the diffuse aurora, *J. Geophys. Res.*, *114*, A07218, doi:10.1029/2009JA014230.

Nakamura, R., W. Baumjohann, R. Schödel, M. Brittnacher, V. A. Sergeev, M. Kubyshkina, T. Mukai, and K. Liou (2001), Earthward flow bursts, auroral streamers, and small expansions, *J. Geophys. Res.*, *106*(A6), 10,791–10,802, doi:10.1029/2000JA000306.

Newell, P. T., T. Sotirelis, and S. Wing (2009), Diffuse, monoenergetic, and broadband aurora: The global precipitation budget, *J. Geophys. Res.*, *114*, A09207, doi: 10.1029/2009JA014326.

Newell, P. T., T. Sotirelis, and S. Wing (2010), Seasonal variations in diffuse, monoenergetic, and broadband aurora, *J. Geophys. Res.*, *115*, A03216, doi:10.1029/2009JA014805.

Ni, B., R. Thorne, J. Liang, V. Angelopoulos, C. Cully, W. Li, X. Zhang, M. Hartinger, O. Le Contel, and A. Roux (2011a), Global distribution of electrostatic electron cyclotron harmonic waves observed on THEMIS, *Geophys. Res. Lett.*, *38*, L17105, doi:10.1029/2011GL048793.

Ni, B., R. M. Thorne, N. P. Meredith, R. B. Horne, and Y. Shprits (2011b), Resonant scattering of plasma sheet electrons leading to diffuse auroral precipitation: 2. Evaluation for whistler-mode chorus waves, *J. Geophys. Res.*, *116*, A04219, doi:10.1029/2010JA016233.

Ni, B., J. Liang, R. M. Thorne, V. Angelopoulos, R. B. Horne, M. Kubyshkina, E. Spanswick, E. F. Donovan, and D. Lummerzheim (2012), Efficient diffuse auroral electron scattering by electrostatic electron cyclotron harmonic waves in the outer magnetosphere: A detailed case study, *J. Geophys. Res.*, *117*, A01218, doi:10.1029/2011JA017095.

Nishimura, Y., L. Lyons, S. Zou, V. Angelopoulos, and S. Mende (2010), Substorm triggering by new plasma intrusion: THEMIS all-sky imager observations, *J. Geophys. Res.*, *115*, A07222, doi:10.1029/2009JA015166.

Roeder, J. L., and H. C. Koons (1989), A survey of electron cyclotron waves in the magnetosphere and the diffuse auroral electron precipitation, *J. Geophys. Res.*, *94*(A3), 2529–2541, doi:10.1029/JA094iA03p02529.

Rönnmark, K., and P. J. Christiansen (1981), Dayside electron cyclotron harmonic emissions, *Nature*, *294*, 335–338.

Roux, A., O. Le Contel, C. Coillot, A. Bouabdellah, B. de la Porte, D. Alison, S. Ruocco, and M. C. Vassal (2008), The search coil magnetometer for THEMIS, *Space Sci. Rev.*, *141*, 265–275, doi:10.1007/s11214-008-9455-8.

Sibeck, D. G., and V. Angelopoulos (2008), THEMIS science objectives and mission phases, *Space Sci. Rev.*, *141*, 35–59, doi:10.1007/s11214-008-9393-5.

Tao, X., R. M. Thorne, W. Li, B. Ni, N. P. Meredith, and R. B. Horne (2011), Evolution of electron pitch-angle distributions following injection from the plasma sheet, *J. Geophys. Res.*, *116*, A04229, doi:10.1029/2010JA016245.

Thorne, R. M., B. Ni, X. Tao, R. B. Horne, and N. P. Meredith (2010), Scattering by chorus waves as the dominant cause of diffuse auroral precipitation, *Nature*, *467*, 943–946, doi:10.1038/nature09467.

Zhang, X.-J., and V. Angelopoulos (2014), On the relationship of electrostatic cyclotron harmonic emissions with electron injections and dipolarization fronts, *J. Geophys. Res. Space Physics*, *119*, 2536–2549, doi:10.1002/2013JA019540.

Zhang, X.-J., V. Angelopoulos, B. Ni, R. M. Thorne, and R. B. Horne (2013), Quasi-steady, marginally unstable electron cyclotron harmonic wave amplitudes, *J. Geophys. Res. Space Physics*, *118*, 3165–3172, doi:10.1002/jgra.50319.